Nano Research

Open Access

Research Article

Atomically precise Pd_8 nanocluster encapsulated in a hierarchically engineered nanoreactor towards enhanced catalysis

Hui Yang[1,§], Yi-Ming Li[1,2,§] ✉, Jinhui Hu[1], Dongxia Shi[1], Yongkang Ge[1], Jiwei Feng[1], Hongting Sheng[1] ✉, and Manzhou Zhu[1,2] ✉

[1] *Department of Chemistry and Centre for Atomic Engineering of Advanced Materials, Anhui Province Key Laboratory of Chemistry for Inorganic/Organic Hybrid Functionalized Materials, Key Laboratory of Structure and Functional Regulation of Hybrid Materials of Ministry of Education, Anhui University, Hefei 230601, China*

[2] *School of Chemistry and Materials Engineering, Anhui Provincial Key Laboratory of Green Carbon Chemistry, Fuyang Normal University, Fuyang 236041, China*

§ *Hui Yang and Yi-Ming Li contributed equally to this work.*

Cite this article: *Nano Research*, **2025**, *18*, 94907208. https://doi.org/10.26599/NR.2025.94907208

ABSTRACT: Metal-organic frameworks (MOFs) have emerged as superior hosting matrices for atomically precise nanoclusters (NCs) encapsulation, offering excellent physical and chemical protections for advanced catalysis. Nevertheless, the MOF coating significantly reduces the NC catalytic efficiency due to the diffusion barriers and the confined microenvironments. Herein, a hierarchically engineered MOF nanoreactor was constructed by controlled structural etching for NC immobilization. This nanoreactor possesses hierarchical pores to accelerate the diffusion rate of reactants and creates hollow structures to unleash the confined NC molecules from the rigid MOF network to a capacious microenvironment. The enhanced mass transfer, improved freedom of NCs, and outstanding stability collectively boosted the catalytic activity of the nanoreactor. By controlling the etching time, freestanding Pd_8@zeolitic imidazolate framework-8 (ZIF-8)-TA_{10} displayed a catalytic efficiency that was 3.17 times greater than that of the initial confined Pd_8@ZIF-8 and even better than free Pd_8. This work opens a new strategy to reduce the inherent limitations of porous matrixes for developing high-performance catalysts.

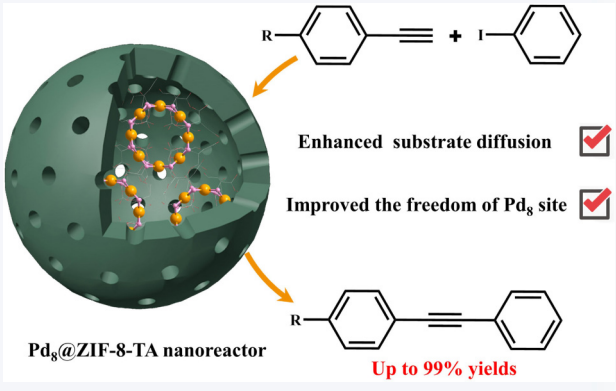

KEYWORDS: metal nanoclusters, metal-organic frameworks, zeolitic imidazolate framework-8 (ZIF-8), hierarchical pores, nanoreactor

1 Introduction

Atomically precise metal nanoclusters (NCs), composed of a few to hundreds of metal atoms and protected ligands, have emerged as a novel and promising nanomaterial in many fields [1–3]. Notably, their ultrasmall sizes and crystallographically defined structures allow the in-depth decipherment of the fundamentals of catalysis [4–9]. One approach to improve the stability, monodispersity, and recyclability of NCs during the reaction is to immobilize them with specific supports. Metal-organic frameworks (MOFs) are an emerging class of porous network materials with precisely determined structures and modifiable pores, allowing them to be excellent hosts for NC immobilization [10–13]. Confining NC in MOFs has shown excellent prospects since it provides NCs with well-defined and optimizable inner-surface microenvironments [14–21]. For example, the encapsulation of Pt_{12} within zeolitic imidazolate framework-8 (ZIF-8) significantly improves NC stability, which could prevent Pt_{12} from aggregating even after the ligand removal [22]. Jiang and co-workers reported the optimization of NC activity by MOF pore microenvironments, highlighting the interfacial interactions between MOFs and NCs [23]. Other studies also showcase the synergistic effects of NC-MOF composites for enhancing their catalytic performance [24–30]. Despite these merits, most confined NCs in MOFs still confront

Received: November 8, 2024; **Revised:** December 17, 2024
Accepted: December 20, 2024

✉Address correspondence to Yi-Ming Li, ymli_chem@163.com; Hongting Sheng, shenght@ahu.edu.cn; Manzhou Zhu, zmz@ahu.edu.cn

significant challenges. For instance, MOFs that are commonly used in encapsulated NCs possess relatively small pore apertures (less than 1 nm), limiting the mass transfer significantly [31, 32]. Moreover, the rigid MOF framework spatially wraps around and confines the immobilized NCs, which provides NC with a specific interfacial interaction, while such interactions significantly alter the NC electron density and activity [23, 33]. Exploring new platforms to overcome these challenges and improve the catalytic performance of embedded NC further is in urgent demand.

MOF nanoreactor that contains hierarchical mesopores and macro-voids within MOF crystals exhibits excellent potential for NC encapsulation, which enables the more effective mass transfer, the relative freestanding state of immobilized NCs, thereby reducing interfacial interactions [34–37]. There have been many strategies for producing hierarchical pores or defects inside microporous MOFs, such as template-directed strategy, modulator-induced method, and perturbation-assisted approach [38–43]. However, these methods often lead to the partial amorphization of MOFs. Etching microporous MOFs with an etching agent is another excellent approach for creating a hierarchically porous MOF nanoreactor [44, 45]. The weak phenolic acids are one of the soft agents for MOF etching, which partly break the framework structures inside MOF crystals while protecting the MOF surface from structurally collapsing [46, 47]. Encapsulating NC within a hierarchical MOF nanoreactor via etching may open up new opportunities to enhance the performance of immobilized NCs, which is ascribed to the enhanced mass transfer facilitated by the hierarchical mesopores and the release of freestanding NC inside MOF nanoreactor [48]. However, hierarchical MOF nanoreactors have barely been employed as the matrix for NC immobilization to date. Moreover, unleashing NC within a MOF nanoreactor also provides a further way to understand and regulate the interfacial interactions between MOFs and NCs, which is essential for the design of functional catalysts.

Herein, a hierarchically porous ZIF nanoreactor containing hollow structures was constructed for the encapsulation of NCs. The Pd_8 was first confined in ZIF-8 via *in situ* encapsulation to form Pd_8@ZIF-8, followed by an etching process to create the large pores and hollow voids inside ZIFs. Besides the higher diffusion barriers, we have provided that the confined Pd_8 in micropore ZIF-8 exhibited strong interfacial interactions, leading to a different electron density from free Pd_8. While hierarchically porous ZIF-8-TA provided freestanding Pd_8 with a capacious microenvironment, significantly reducing the interactions and recovering the same electron density as their free counterpart. Such ZIF-8-TA nanoreactor enhanced the stability and recyclability of immobilized Pd_8 while facilitating the mass transfer and weakening the interfacial interaction, thereby showing 3.17 times higher catalytic efficiency than confined Pd_8@ZIF-8.

2 Experimental

2.1 Synthesis of Pd_8 NC

67.5 mg of $Pd(OAc)_2$ (0.3 mmol) and 225 mg of mercaptosuccinic acid (MSA, 1.5 mmol) were added in an agate mortar and continuously ground for 15 min until the color of the solid powder changed from white to yellow. 60 mg of $NaBH_4$ (1.5 mmol) was added to the mixture and further ground for 30 min until the powder became dark. Subsequently, 3 mL of H_2O was added to the mixture. The solution was collected and washed with ethanol (EtOH) to remove excess MSA. Then, 2 mL of H_2O was added to disperse the precipitate and aged at room temperature for 24 h. Finally, the precipitate was removed by centrifugation (12,000 rpm, 5 min) and the supernatant was washed with ethanol, and the obtained precipitate was dried under vacuum.

2.2 Synthesis of ZIF-8

An aqueous solution of $Zn(NO_3)_2{\cdot}6H_2O$ (1.5 mL, 50 $g{\cdot}L^{-1}$) was added to 20 mL H_2O, followed by the addition of the H_2O solution containing 2-methylimidazole (9 mL, 200 $g{\cdot}L^{-1}$). After stirring for 5 min, 2 mL aqueous solution of cetyltrimethylammonium bromide (CTAB, 50 $g{\cdot}L^{-1}$) was added to the mixture and stirred overnight. The resulting white powder was separated by centrifugation (8500 rpm, 5 min), washed three times with ultrapure water, and dried under vacuum at 35 °C.

2.3 Synthesis of Pd_8@ZIF-8

Pd_8@ZIF-8 was synthesized *via* a similar procedure to pure ZIF-8, besides adding a few Pd_8 solutions (200 μL, 10 $mg{\cdot}mL^{-1}$) to the linker's solution. Pd_8@ZIF-8 could be obtained within 3 h, followed by centrifugation-wash cycles.

2.4 Synthesis of Pd_8@ZIF-8-TA_n (*n* represented the etching time, min)

Tannic acid solution (TA, 5 $mg{\cdot}mL^{-1}$) was first prepared, followed by adding 50 mg Pd_8@ZIF-8. The solution was left to stand at room temperature for the desired time. The resulting powder was centrifuged and washed with ultrapure water 2 times, followed by methanol (MeOH) 3 times, and dried under vacuum at 35 °C.

2.5 Sonogashira coupling reaction

112 μL iodobenzene (1.0 mmol), 415 μL pyrrolidine (5 mmol), 131 μL phenylacetylene (1.2 mmol), and 1.66×10^{-4} mmol catalyst (based on Pd) were added to a Schlenk reaction flask containing 2.5 mL of deionized water. The reaction mixture was stirred under the protection of N_2 in an oil bath at 60 °C for a certain time. The mixture was extracted with ethyl acetate, and the supernatant obtained was determined by gas chromatography. The catalyst was recovered by washing with ethanol and dried under vacuum at room temperature overnight.

2.6 Reduction of *p*-nitrophenol (4-NP)

2.5×10^{-5} mmol of catalyst was added to a $NaBH_4$ solution (0.5 $mg{\cdot}mL^{-1}$), followed by the introduction of 100 μL of *p*-nitrophenol solution (33.3 $mmol{\cdot}L^{-1}$), and the reaction was stirred at room temperature and monitored by ultraviolet–visible (UV–vis) spectrum.

3 Results and discussion

Pd_8 NC was verified by the UV–vis spectrum, transmission electron microscopy (TEM) images, Fourier transform infrared (FTIR) spectrum, X-ray photoelectron spectroscopy (XPS), and thermogravimetric analysis (TGA, Figs. S1–S5 in the Electronic Supplementary Material (ESM)) [49]. The encapsulation of Pd_8 inside ZIF-8 was carried out in the presence of ZIF precursor and Pd_8 solution. The as-obtained Pd_8@ZIF-8 was next etched by TA (5 $mg{\cdot}mL^{-1}$) for 10 min to acquire hierarchically porous ZIFs with hollow structures to release the confined NC molecules, called Pd_8@ZIF-8-TA_{10} nanoreactor (10 represents etching for 10 min,

Scheme 1). Pd_8 NC did not leach from the nanoreactor during the etching process since the outer parts of ZIF-8 provided maintenance (Fig. S6 in the ESM). Wide angle X-ray scattering (WAXS) and powder X-ray diffraction (PXRD) patterns demonstrated the successful preparation of the Pd_8@ZIF-8 catalyst, and the introduction of Pd_8 did not affect the formation of the ZIF shell (Fig. 1(a) and Fig. S7 in the ESM). In addition, the WAXS and PXRD patterns of Pd_8@ZIF-8-TA_{10} matched well with that of Pd_8@ZIF-8, suggesting that the etching process by TA did not affect the long-range ZIF-8 crystal structure. The N_2 uptake data at 77 K of ZIF-8, ZIF-8-TA, Pd_8@ZIF-8, and Pd_8@ZIF-8-TA_{10} were collected. Pd_8@ZIF-8 exhibited a lower surface area than pure ZIF-8, probably due to the occupation of Pd_8 within the ZIF crystals, emphasizing the successful immobilization of Pd_8 (Fig. 1(b) and Figs. S8–S10 in the ESM). Furthermore, the surface area severely decreased after the etching process (Pd_8@ZIF-8: 1100.1 $m^2 \cdot g^{-1}$; Pd_8@ZIF-8-TA_{10}: 722.2 $m^2 \cdot g^{-1}$), which was similar to previous reports [42]. The etching process destroys part of the microporous structure of the ZIF skeleton, leading to the generation of hierarchical pores and hollow structures, as confirmed by the hysteresis loop of hollow Pd_8@ZIF-8-TA_{10} in the nitrogen isothermal sorption profiles.

The etching effect of TA on Pd_8@ZIF-8 was next explored. For Pd_8@ZIF-8-TA_{10}, the characteristic FTIR peak at 1700 cm^{-1} was attributed to the stretching vibration of C–O groups of TA, proving that TA would be partially retained in ZIF crystal (Fig. 1(c)). The peak observed at 1600 cm^{-1} was attributed to C=O bonds from the Pd_8 ligand, implying the existence of NC in nanoreactor. The elemental survey from XPS of Pd_8, ZIF-8, Pd_8@ZIF-8, and Pd_8@ZIF-8-TA_{10} was performed. We found much stronger O element signals in Pd_8@ZIF-8-TA_{10} than in Pd_8@ZIF-8, which might be attributed to the residual TA in the nanoreactor (Fig. 1(d)).

Importantly, Pd_8@ZIF-8 exhibited a blue shift of Pd 3d peaks compared to free Pd_8 in XPS data (Fig. 1(e)), indicating a chemical interaction between confined Pd_8 and ZIF-8. The electron density difference between free and confined NCs might be attributed to the confined microenvironment of Pd_8 by ZIF coatings [20, 29]. After the etching process, the freestanding Pd_8@ZIF-8-TA_{10} nanoreactor displayed a similar binding energy of Pd 3d compared to free Pd_8, suggesting that the etching treatment reduced the interfacial interactions between ZIFs and Pd_8. The structural integrity of confined Pd_8@ZIF-8 and freestanding Pd_8@ZIF-8-TA_{10} were also studied. In the UV–vis diffuse reflectance spectra, the characteristic peaks of confined and freestanding Pd_8 were the same as those of free NC (Fig. 1(f)), demonstrating the primal structure of encapsulated Pd_8 was highly preserved. Furthermore, TA did not change the characteristic peaks of Pd_8 NC, suggesting that the etching procedure did not affect the NC structure (Fig. S11 in the ESM).

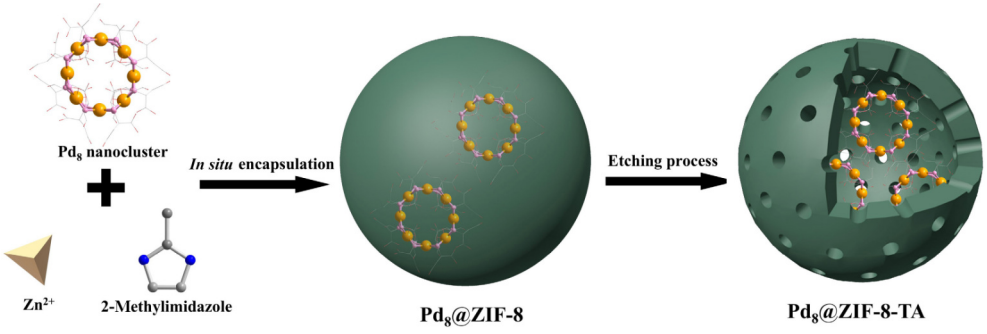

Scheme 1 Synthetic route to Pd_8@ZIF-8-TA nanoreactor.

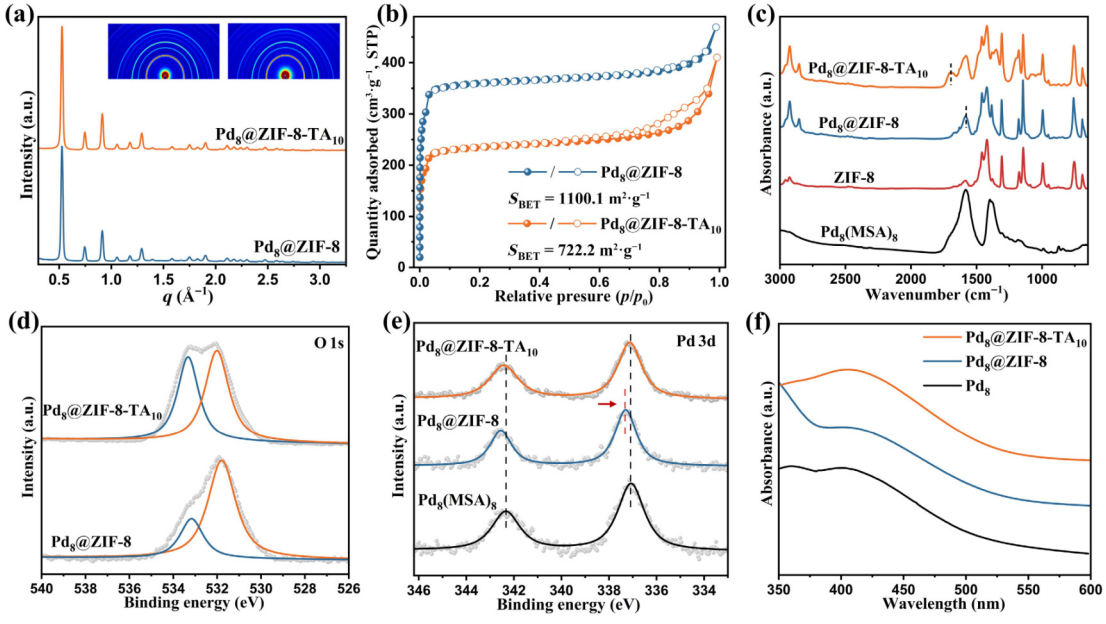

Figure 1 (a) WAXS patterns of Pd_8@ZIF-8 and Pd_8@ZIF-8-TA_{10}. (b) N_2 adsorption/desorption isotherms (77 K) of Pd_8@ZIF-8 and Pd_8@ZIF-8-TA_{10}. (c) FTIR data of Pd_8@ZIF-8 and Pd_8@ZIF-8-TA_{10}. XPS spectra of (d) O 1s and (e) Pd 3d of Pd_8@ZIF-8 and Pd_8@ZIF-8-TA_{10}. (f) UV–vis spectra of Pd_8@ZIF-8 and Pd_8@ZIF-8-TA_{10}.

The morphological structure of Pd_8@ZIF-8 and Pd_8@ZIF-8-TA_{10} were next investigated through TEM and high-angle annular dark-field scanning TEM (HAADF-STEM). As shown in Figs. 2(a) and 2(b), Pd_8@ZIF-8-TA_{10} clearly showed the central cavity formation after TA treatment, which was different from solid Pd_8@ZIF-8 bearing a microporous internal structure. Furthermore, the HAADF-TEM images verified the uniform dispersion of the confined and freestanding Pd_8 in all samples (Figs. 2(c) and 2(d)). No significant changes in NC size were found (Figs. S12 and S13 in the ESM), revealing that neither the immobilization nor etching processes changed the geometric structure of Pd_8 NC.

The hierarchical and hollow structure accelerates the diffusion of reactants/products inside ZIF crystals. It unleashes confined NCs to a capacious microenvironment with reduced interfacial interactions, thereby greatly enhancing their catalytic performance. Free Pd_8, solid Pd_8@ZIF-8, and hollow Pd_8@ZIF-8-TA_{10} were applied as catalysts in the Sonogashira coupling reaction, and the optimal conditions for reactions were first screened. Several solvents (such as H_2O, EtOH, MeOH, N,N-dimethylformamide (DMF), acetonitrile (MeCN), and tetrahydrofuran (THF)) were tested, and H_2O showed the best catalytic performance with a yield of 76.2% (Table S1 in the ESM, entries 1–6). Compared to inorganic bases such as K_2CO_3, Cs_2CO_3, etc., organic bases showed much better conversions, and pyrrolidine was the most suitable base for the reaction (Table S1 in the ESM, entries 7–13). The reaction temperatures were the other factor that affected the reaction progress. Our data showed that the optimal temperature was 60 °C. Lower temperatures offered unsatisfactory yields, while higher temperatures gave negligible improvements in conversions (Table S1 in the ESM, entries 14 and 15). Furthermore, no products were found when pure ZIF-8, TA, or ZIF-8-TA were used as catalysts, indicating that the catalyst activity was derived from the intrinsic activity of encapsulated Pd_8 (Table S1 in the ESM, entries 16–18). Free Pd_8, Pd_8@ZIF-8, and Pd_8@ZIF-8-TA_{10} could catalyze the reaction under optimal conditions, while Pd_8@ZIF-8-TA_{10} exhibited the best conversion (Table S1 in the ESM, entries 19–21). The activity of Pd_8@ZIF-8-TA_{10} was better than the free Pd_8 NC, which was attributed to the improved stability of Pd_8 NC (Fig. S14 in the ESM).

The effect of etching time on the Pd_8@ZIF-8-TA nanoreactor activity was then explored. PXRD patterns of Pd_8@ZIF-8-TA at different times showed no additional diffraction peak from impurities (Fig. 3(a)), implying that prolonging the TA etching time did not affect the pristine crystal structure of ZIF-8. The catalytic performances of free Pd_8, Pd_8@ZIF-8, and Pd_8@ZIF-8-TA_n (n represents the etching time) were next investigated. Interestingly, a nonlinear correlation between the etching time and the activity of the Pd_8@ZIF-8-TA_n nanoreactor was obtained. The catalytic performance of Pd_8@ZIF-8-TA_n was first improved and then decreased with the extension of etching time. The best conversion was obtained by etching Pd_8@ZIF-8 for 10 min (Fig. 3(b)). This might be attributed to the improvement of diffusion efficiency and degree of freedom brought about by early etching (< 10 min) and the decrease in stability of immobilized NC caused by excessive etching after 10 min.

Under the optimized conditions, the kinetics of Pd_8@ZIF-8 and Pd_8@ZIF-8-TA_{10} were investigated in detail. After 6 h, Pd_8@ZIF-8-TA_{10} provided 72.6% conversion, which was more than two times higher than that of unetched Pd_8@ZIF-8 (32.4%). Prolonging reaction time to 24 h, Pd_8@ZIF-8 still could not achieve quantitative conversion, which was achieved with Pd_8@ZIF-8-TA_{10} after 10 h (Fig. 3(c)). The catalytic rate constant of Pd_8@ZIF-8-TA_{10} was calculated to be 0.2496 h^{-1} (Fig. 3(d)), which was 3.17 times higher than that of Pd_8@ZIF-8 (0.0786 h^{-1}), demonstrating the superior activity of Pd_8@ZIF-8-TA_{10} nanoreactor compared to parental Pd_8@ZIF-8. Furthermore, changing the functional groups of reactants did not affect the catalytic performance of the nanoreactor. Pd_8@ZIF-8-TA_{10} showed 2.2–2.6 times higher conversions than Pd_8@ZIF-8 (Fig. 3(e)), suggesting the high

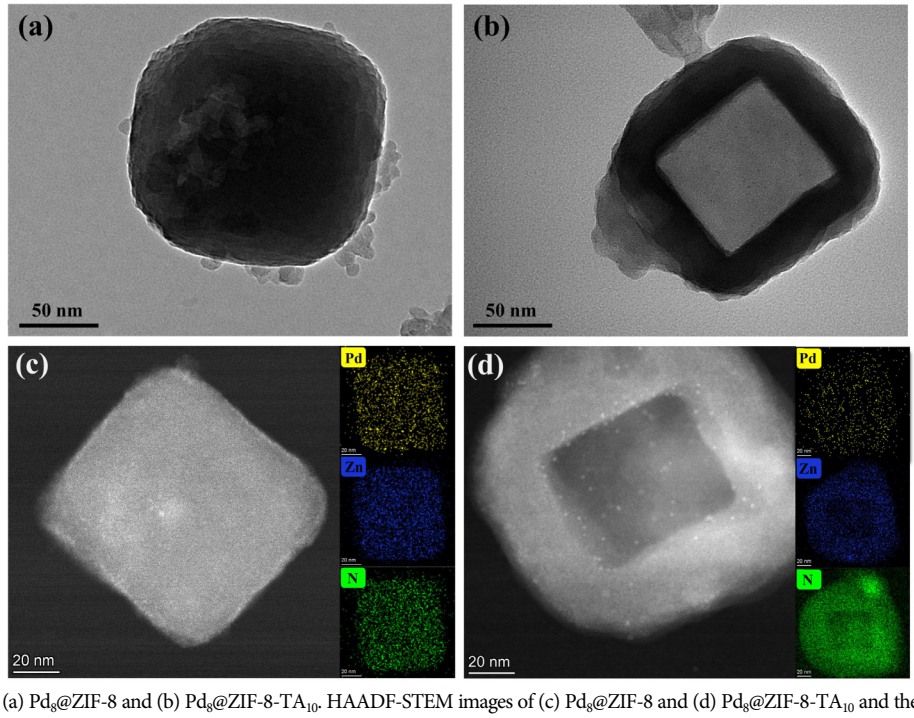

Figure 2 TEM images of (a) Pd_8@ZIF-8 and (b) Pd_8@ZIF-8-TA_{10}. HAADF-STEM images of (c) Pd_8@ZIF-8 and (d) Pd_8@ZIF-8-TA_{10} and their corresponding elemental mappings.

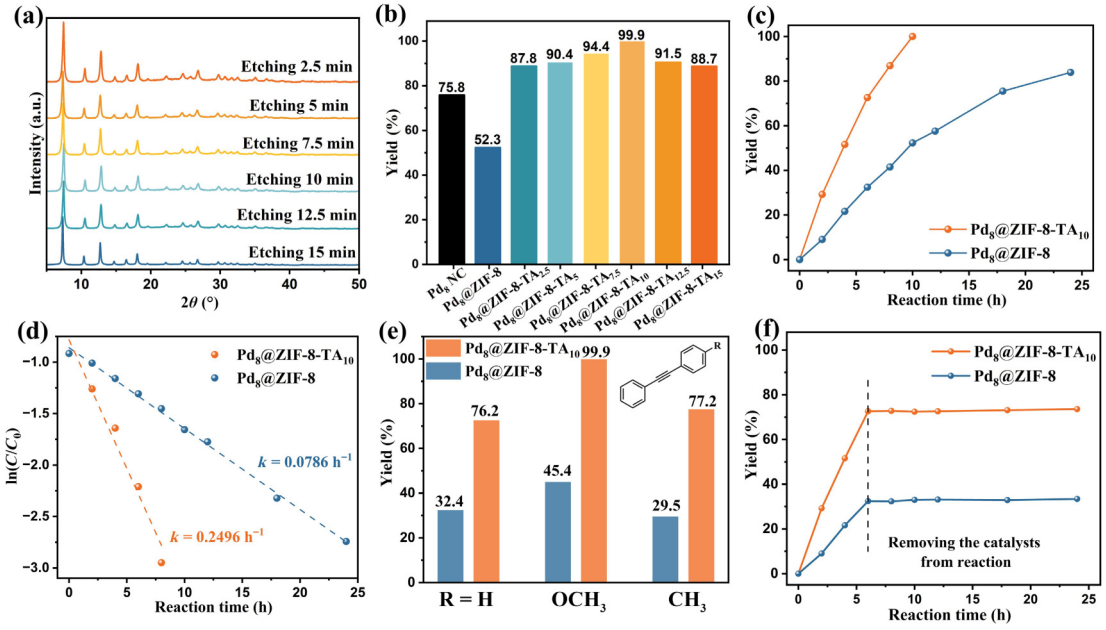

Figure 3 (a) PXRD patterns of Pd_8@ZIF-8-TA_{10} with different etching times. (b) The catalytic performances of Pd_8, Pd_8@ZIF-8, and Pd_8@ZIF-8-TA_{10} with different etching times. (c) The conversion rate curves of Pd_8@ZIF-8 and Pd_8@ZIF-8-TA_{10} in 24 h. (d) C/C_0 curves of the reactant catalyzed by Pd_8@ZIF-8 and Pd_8@ZIF-8-TA_{10} (C and C_0 represent the concentrations of reactant with time and initial stage). (e) The catalytic performances of Pd_8@ZIF-8 and Pd_8@ZIF-8-TA_{10} towards various reactants with different groups. (f) The thermal filtration experiments of Pd_8@ZIF-8 and Pd_8@ZIF-8-TA_{10}.

tolerance of our nanoreactor to various reactants. The thermal filtration experiments showed that after removing the Pd_8@ZIF-8 and Pd_8@ZIF-8-TA_{10} catalysts from the reaction, no further increase in products was observed (Fig. 3(f)). The filtrate after the reaction was also analyzed by inductively coupled plasma-optical emission spectroscopy (ICP-OES), providing no leaching of Pd ions from the catalysts (< 0.0001%). These results together confirmed the heterogeneous nature of both Pd_8@ZIF-8 and Pd_8@ZIF-8-TA_{10} as catalysts.

The typical reduction reaction of 4-NP was also performed using Pd_8@ZIF-8 and Pd_8@ZIF-8-TA_{10} as catalysts to evaluate their catalytic performances further. As shown in Figs. 4(a) and 4(b), Pd_8@ZIF-8-TA_{10} completely reduced 4-NP within 25 min, while Pd_8@ZIF-8 only gave about half of the total conversion at the same time, indicating the superior catalytic performance of Pd_8@ZIF-8-TA_{10} nanoreactor. In addition, both the Pd_8@ZIF-8 and Pd_8@ZIF-8-TA_{10} could be recycled at least 5 times without a noticeable loss of activity (Fig. 4(c)). PXRD data showed no apparent change in nanoreactor crystallinity after the reaction (Fig. 4(d)). TEM images, UV–vis spectra, and N_2 uptake measurement showed no significant change before and after the reaction (Figs. S15–S17 in the ESM), suggesting the excellent recyclability and stability of nanoreactor.

4 Conclusions

In summary, we have created a facile etching strategy to encapsulate NC into hierarchically porous and hollow MOF nanoreactors with significantly enhanced catalytic performance. The etching process partially broke the internal pore of ZIFs to unleash the confined NC within the hollow structure, while the crystal surface was highly maintained to keep the heterogeneous nature of the nanoreactor. The Pd_8@ZIF-8-TA nanoreactor can facilitate the diffusion of the reactants and products, provide more capacious internal environments for NC, and stabilize NC to enhance their recyclability. By fine-tuning the etching process, freestanding Pd_8 in hollow Pd_8@ZIF-8-TA_{10} nanoreactor exhibited a 3.17-fold enhancement in catalytic performance compared to confined Pd_8 in unetched Pd_8@ZIF-8, even better than its free counterparts. This work provides a new strategy for constructing a high-active nanoreactor to encapsulate the freestanding NC in hollow MOFs.

Electronic Supplementary Material: Supplementary material (UV–vis spectra, TEM and HAADF-STEM images, XPS spectra, FTIR data, N_2 adsorption/desorption measurements, and ^{1}H-NMR data) is available in the online version of this article at https://doi.org/10.26599/NR.2025.94907208.

Data availability

All data needed to support the conclusions in the paper are presented in the manuscript and the Electronic Supplementary Material. Additional data related to this paper may be requested from the corresponding author upon request.

Acknowledgements

We acknowledge financial support by the National Natural Science Foundation of China (Nos. 22305003 and 21972001) and the China Postdoctoral Science Foundation (No. 2023M740009).

Declaration of competing interest

All the contributing authors report no conflict of interests in this work.

Author contribution statement

H. Y.: Data curation, validation. Y.-M. L.: Experimental design, project administration, writing manuscript, funding acquisition. J. H. H.: Experimental design, project administration. D. X. S.: Data curation, validation. Y. K. G.: Validation. J. W. F.: Validation. H. T.

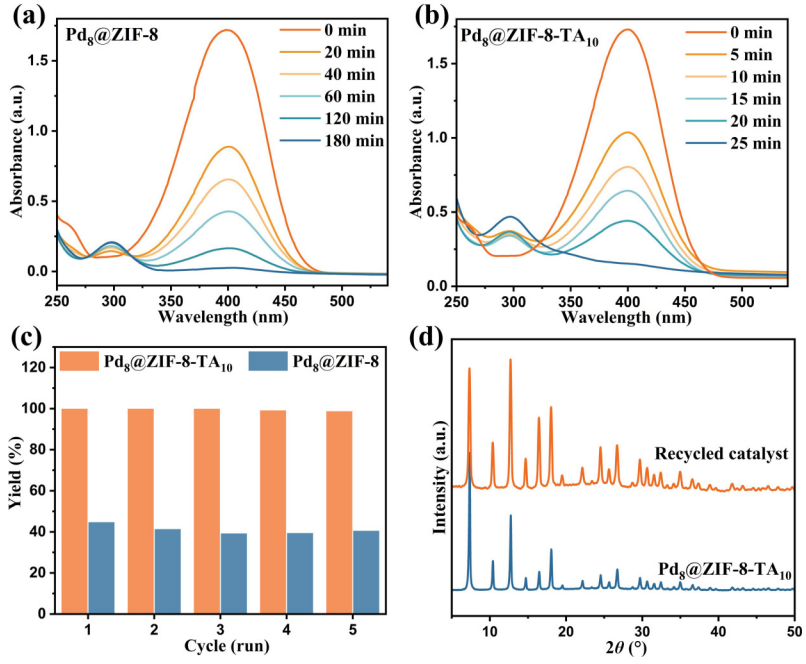

Figure 4 UV–vis absorption spectra of the 4-NP reduction by $NaBH_4$ as reducing agent with (a) Pd_8@ZIF-8 and (b) Pd_8@ZIF-8-TA_{10}. (c) Recycling experiments for Pd_8@ZIF-8 and Pd_8@ZIF-8-TA_{10}. (d) PXRD patterns for recycled Pd_8@ZIF-8-TA_{10}.

S.: Project administration, writing manuscript, funding acquisition. M. Z. Z.: Project administration, funding acquisition. All the authors have approved the final manuscript.

Use of AI statement

None.

References

[1] Wang, X. J.; Yin, B.; Jiang, L. R.; Yang, C.; Liu, Y.; Zou, G.; Chen, S.; Zhu, M. Z. Ligand-protected metal nanoclusters as low-loss, highly polarized emitters for optical waveguides. *Science* **2023**, *381*, 784–790.

[2] Jing, W. T.; Shen, H.; Qin, R. X.; Wu, Q. Y.; Liu, K. L.; Zheng, N. F. Surface and interface coordination chemistry learned from model heterogeneous metal nanocatalysts: From atomically dispersed catalysts to atomically precise clusters. *Chem. Rev.* **2023**, *123*, 5948–6002.

[3] Jin, R. C.; Li, G.; Sharma, S.; Li, Y. W.; Du, X. S. Toward active-site tailoring in heterogeneous catalysis by atomically precise metal nanoclusters with crystallographic structures. *Chem. Rev.* **2021**, *121*, 567–648.

[4] Du, Y. X.; Sheng, H. T.; Astruc, D.; Zhu, M. Z. Atomically precise noble metal nanoclusters as efficient catalysts: A bridge between structure and properties. *Chem. Rev.* **2020**, *120*, 526–622.

[5] Zheng, K.; Zhang, J. W.; Zhao, D.; Yang, Y.; Li, Z. M.; Li, G. Motif-mediated $Au_{25}(SPh)_5(PPh_3)_{10}X_2$ nanorods with conjugated electron delocalization. *Nano Res.* **2019**, *12*, 501–507.

[6] Liu, Y. Y.; Chai, X. Q.; Cai, X.; Chen, M. Y.; Jin, R. C.; Ding, W. P.; Zhu, Y. Central doping of a foreign atom into the silver cluster for catalytic conversion of CO_2 toward C–C bond formation. *Angew. Chem., Int. Ed.* **2018**, *57*, 9775–9779.

[7] Guan, Z. J.; He, R. L.; Yuan, S. F.; Li, J. J.; Hu, F.; Liu, C. Y.; Wang, Q. M. Ligand engineering toward the trade-off between stability and activity in cluster catalysis. *Angew. Chem., Int. Ed.* **2022**, *61*, e202116965.

[8] Zhang, Y. F.; Gu, X. R.; Busari, F. K.; Barkaoui, S.; Han, Z. K.; Baiker, A.; Zhao, Z.; Li, G. Size hierarchy of gold clusters in nanogold-catalyzed acetylene hydrochlorination. *Nano Res.* **2024**, *17*, 9594–9600.

[9] Qin, Z. X.; Hu, S.; Han, W. H.; Li, Z. W.; Xu, W. W.; Zhang, J. J.; Li, G. Tailoring optical and photocatalytic properties by single-Ag-atom exchange in $Au_{13}Ag_{12}(PPh_3)_{10}Cl_8$ nanoclusters. *Nano Res.* **2022**, *15*, 2971–2976.

[10] Yuan, S.; Feng, L.; Wang, K. C.; Pang, J. D.; Bosch, M.; Lollar, C.; Sun, Y. J.; Qin, J. S.; Yang, X. Y.; Zhang, P. et al. Stable metal-organic frameworks: Design, synthesis, and applications. *Adv. Mater.* **2018**, *30*, 1704303.

[11] Yang, Q. H.; Xu, Q.; Jiang, H. L. Metal-organic frameworks meet metal nanoparticles: Synergistic effect for enhanced catalysis. *Chem. Soc. Rev.* **2017**, *46*, 4774–4808.

[12] Shen, Y.; Pan, T.; Wang, L.; Ren, Z.; Zhang, W. N.; Huo, F. W. Programmable logic in metal-organic frameworks for catalysis. *Adv. Mater.* **2021**, *33*, 2007442.

[13] Li, Y. M.; Yuan, J.; Ren, H.; Ji, C. Y.; Tao, Y.; Wu, Y. H.; Chou, L. Y.; Zhang, Y. B.; Cheng, L. Fine-tuning the micro-environment to optimize the catalytic activity of enzymes immobilized in multivariate metal-organic frameworks. *J. Am. Chem. Soc.* **2021**, *143*, 15378–15390.

[14] Kollmannsberger, K. L.; Kronthaler, L.; Jinschek, J. R.; Fischer, R. A. Defined metal atom aggregates precisely incorporated into metal-organic frameworks. *Chem. Soc. Rev.* **2022**, *51*, 9933–9959.

[15] Li, Y. M.; Hu, J. H.; Zhu, M. Z. Confining atomically precise nanoclusters in metal-organic frameworks for advanced catalysis. *Coord. Chem. Rev.* **2023**, *495*, 215364.

[16] Luo, L. S.; Jin, R. C. Atomically precise metal nanoclusters meet metal-organic frameworks. *iScience* **2021**, *24*, 103206.

[17] Luo, Y. C.; Fan, S. Y.; Yu, W. Q.; Wu, Z. L.; Cullen, D. A.; Liang, C. L.; Shi, J. Y.; Su, C. Y. Fabrication of $Au_{25}(SG)_{18}$-ZIF-8 nanocomposites: A facile strategy to position $Au_{25}(SG)_{18}$ nanoclusters inside and outside ZIF-8. *Adv. Mater.* **2018**, *30*, 1704576.

[18] Zhu, Y. F.; Qiu, X. Y.; Zhao, S. L.; Guo, J.; Zhang, X. F.; Zhao, W. S.; Shi, Y. N.; Tang, Z. Y. Structure regulated catalytic performance

of gold nanocluster-MOF nanocomposites. *Nano Res.* **2020**, *13*, 1928–1932.

[19] Guo, J.; Wan, Y.; Zhu, Y. F.; Zhao, M. T.; Tang, Z. Y. Advanced photocatalysts based on metal nanoparticle/metal-organic framework composites. *Nano Res.* **2021**, *14*, 2037–2052.

[20] Wang, N.; Sun, Q. M.; Yu, J. H. Ultrasmall metal nanoparticles confined within crystalline nanoporous materials: A fascinating class of nanocatalysts. *Adv. Mater.* **2019**, *31*, 1803966.

[21] Cao, J.; Yang, Z. H.; Xiong, W. P.; Zhou, Y. Y.; Wu, Y.; Jia, M. Y.; Zhou, C. Y.; Xu, Z. Y. Ultrafine metal species confined in metal-organic frameworks: Fabrication, characterization and photocatalytic applications. *Coord. Chem. Rev.* **2021**, *439*, 213924.

[22] Kratzl, K.; Kratky, T.; Günther, S.; Tomanec, O.; Zbořil, R.; Michalička, J.; Macak, J. M.; Cokoja, M.; Fischer, R. A. Generation and stabilization of small platinum clusters $Pt_{12\pm x}$ inside a metal-organic framework. *J. Am. Chem. Soc.* **2019**, *141*, 13962–13969.

[23] Wang, H.; Liu, X. Y.; Yang, W. J.; Mao, G. Y.; Meng, Z.; Wu, Z. K.; Jiang, H. L. Surface-clean Au_{25} nanoclusters in modulated microenvironment enabled by metal-organic frameworks for enhanced catalysis. *J. Am. Chem. Soc.* **2022**, *144*, 22008–22017.

[24] Zheng, F. Q.; Fan, Y. J.; Chen, W. Homogeneous distribution of $Pt_{16}(C_4O_4SH_5)_{26}$ clusters in ZIF-67 for efficient hydrogen generation and oxygen reduction. *ACS Appl. Mater. Interfaces* **2021**, *13*, 38170–38178.

[25] Zhang, J.; Cui, X. F.; Zhou, Y.; Kong, T. T.; Wang, Y. X.; Wei, X. W.; Xiong, Y. J. Enhancing the durability of Au clusters in CO_2 photoreduction via encapsulation in Cu-based metal-organic frameworks. *Chem. Commun.* **2023**, *59*, 2299–2302.

[26] Yun, Y. P.; Sheng, H. T.; Bao, K.; Xu, L.; Zhang, Y.; Astruc, D.; Zhu, M. Z. Design and remarkable efficiency of the robust sandwich cluster composite nanocatalysts ZIF-8@Au_{25}@ZIF-67. *J. Am. Chem. Soc.* **2020**, *142*, 4126–4130.

[27] Wang, H.; Zhang, X. Y.; Zhang, W.; Zhou, M.; Jiang, H. L. Heteroatom-doped Ag_{25} nanoclusters encapsulated in metal-organic frameworks for photocatalytic hydrogen production. *Angew. Chem., Int. Ed.* **2024**, *63*, e202401443.

[28] Yao, A. M.; Du, Y. X.; Han, M.; Wang, Y.; Hu, J. S.; Zhu, Q. T.; Sheng, H. T.; Zhu, M. Z. Covalence bridge atomically precise metal nanocluster and metal-organic frameworks for enhanced photostability and photocatalysis. *Nano Res.* **2023**, *16*, 1527–1532.

[29] Jiang, Y. L.; Yu, Y.; Zhang, X.; Weinert, M.; Song, X. L.; Ai, J.; Han, L.; Fei, H. H. N-heterocyclic carbene-stabilized ultrasmall gold nanoclusters in a metal-organic framework for photocatalytic CO_2 reduction. *Angew. Chem., Int. Ed.* **2021**, *60*, 17388–17393.

[30] Li, Y. M.; Shi, D. X.; Yuan, J.; Zuo, R. M.; Yang, H.; Hu, J. H.; Hu, S. X.; Sheng, H. T.; Zhu, M. Z. *In situ* encapsulation of atomically precise nanoclusters in reticular frameworks via mechanochemical synthesis. *Adv. Mater.*, in press, DOI: 10.1002/adma.202412768.

[31] Bi, X. Y.; Li, L. B.; Niu, Q. J.; Liu, X. H.; Luo, L. J.; Jiang, H. H.; You, T. Y. Highly fluorescent magnetic ATT-AuNCs@ZIF-8 for all-in-one detection and removal of Hg^{2+}: An ultrasensitive probe to evaluate its removal efficiency. *Inorg. Chem.* **2023**, *62*, 3123–3133.

[32] Nie, Y. M.; Tao, X. L.; Zhang, H. W.; Chai, Y. Q.; Yuan, R. Self-assembly of gold nanoclusters into a metal-organic framework with efficient electrochemiluminescence and their application for sensitive detection of rutin. *Anal. Chem.* **2021**, *93*, 3445–3451.

[33] You, Q.; Wang, H.; Zhao, Y.; Fan, W. T.; Gu, W. M.; Jiang, H. L.; Wu, Z. K. Bottom-up construction of metal-organic framework loricae on metal nanoclusters with consecutive single nonmetal atom tuning for tailored catalysis. *J. Am. Chem. Soc.* **2024**, *146*, 9026–9035.

[34] Li, M. M.; Qiao, S.; Zheng, Y. L.; Andaloussi, Y. H.; Li, X.; Zhang, Z. J.; Li, A.; Cheng, P.; Ma, S. Q.; Chen, Y. Fabricating covalent organic framework capsules with commodious microenvironment for enzymes. *J. Am. Chem. Soc.* **2020**, *142*, 6675–6681.

[35] Chen, S. Y.; Lo, W. S.; Huang, Y. D.; Si, X. M.; Liao, F. S.; Lin, S. W.; Williams, B. P.; Sun, T. Q.; Lin, H. W.; An, Y. Y. et al. Probing interactions between metal-organic frameworks and freestanding enzymes in a hollow structure. *Nano Lett.* **2020**, *20*, 6630–6635.

[36] Liang, J. Y.; Gao, S.; Liu, J.; Zulkifli, M. Y. B.; Xu, J. T.; Scott, J.; Chen, V.; Shi, J. F.; Rawal, A.; Liang, K. Hierarchically porous biocatalytic MOF microreactor as a versatile platform towards enhanced multienzyme and cofactor-dependent biocatalysis. *Angew. Chem., Int. Ed.* **2021**, *60*, 5421–5428.

[37] Sun, Y. Y.; Shi, J. F.; Zhang, S. H.; Wu, Y. Z.; Mei, S.; Qian, W. L.; Jiang, Z. Y. Hierarchically porous and water-tolerant metal-organic frameworks for enzyme encapsulation. *Ind. Eng. Chem. Res.* **2019**, *58*, 12835–12844.

[38] Cai, G. R.; Yan, P.; Zhang, L. L.; Zhou, H. C.; Jiang, H. L. Metal-organic framework-based hierarchically porous materials: Synthesis and applications. *Chem. Rev.* **2021**, *121*, 12278–12326.

[39] Shen, K.; Zhang, L.; Chen, X. D.; Liu, L. M.; Zhang, D. L.; Han, Y.; Chen, J. Y.; Long, J. L.; Luque, R.; Li, Y. et al. Ordered macro-microporous metal-organic framework single crystals. *Science* **2018**, *359*, 206–210.

[40] Li, K.; Yang, J.; Huang, R.; Lin, S. L.; Gu, J. L. Ordered large-pore mesoMOFs based on synergistic effects of triblock polymer and Hofmeister ion. *Angew. Chem., Int. Ed.* **2020**, *59*, 14124–14128.

[41] Cai, G. R.; Jiang, H. L. A modulator-induced defect-formation strategy to hierarchically porous metal-organic frameworks with high stability. *Angew. Chem.* **2017**, *129*, 578–582.

[42] Park, J.; Wang, Z. U.; Sun, L. B.; Chen, Y. P.; Zhou, H. C. Introduction of functionalized mesopores to metal-organic frameworks via metal-ligand-fragment coassembly. *J. Am. Chem. Soc.* **2012**, *134*, 20110–20116.

[43] Yue, Y. F.; Binder, A. J.; Song, R. J.; Cui, Y. J.; Chen, J. H.; Hensley, D. K.; Dai, S. Encapsulation of large dye molecules in hierarchically superstructured metal-organic frameworks. *Dalton Trans.* **2014**, *43*, 17893–17898.

[44] Yuan, S.; Zou, L. F.; Qin, J. S.; Li, J. L.; Huang, L.; Feng, L.; Wang, X.; Bosch, M.; Alsalme, A.; Cagin, T. et al. Construction of hierarchically porous metal-organic frameworks through linker labilization. *Nat. Commun.* **2017**, *8*, 15356.

[45] Feng, L.; Yuan, S.; Zhang, L. L.; Tan, K.; Li, J. L.; Kirchon, A.; Liu, L. M.; Zhang, P.; Han, Y.; Chabal, Y. J. et al. Creating hierarchical pores by controlled linker thermolysis in multivariate metal-organic frameworks. *J. Am. Chem. Soc.* **2018**, *140*, 2363–2372.

[46] Hu, M.; Ju, Y.; Liang, K.; Suma, T.; Cui, J. W.; Caruso, F. Void engineering in metal-organic frameworks via synergistic etching and surface functionalization. *Adv. Funct. Mater.* **2016**, *26*, 5827–5834.

[47] Qiu, J. C.; Lin, Y. R.; Zhang, S. T.; Ma, J.; Zhang, Y.; Yuan, M. W.; Sun, G. B.; Nan, C. Y. Hollow catalysts through different etching treatments to improve active sites and oxygen vacancies for high-performance Li-O_2 battery. *Nano Res.* **2023**, *16*, 6798–6804.

[48] Wang, S. H.; Fan, Y. N.; Teng, J.; Fan, Y. Z.; Jiang, J. J.; Wang, H. P.; Grützmacher, H.; Wang, D. W.; Su, C. Y. Nanoreactor based on macroporous single crystals of metal-organic framework. *Small* **2016**, *12*, 5702–5709.

[49] An, P.; Anumula, R.; Cui, C. N.; Liu, Y.; Zhan, F.; Tao, Y.; Luo, Z. X. A facile method to synthesize water-soluble Pd_8 nanoclusters unraveling the catalytic mechanism of p-nitrophenol to p-aminophenol. *Nano Res.* **2019**, *12*, 2589–2596.